Split-vacancy defect complexes of oxygen in hcp and fcc cobalt

Shreyas J. Honrao,[1,2] Quentin Rizzardi,[3] Robert Maaß,[3,4] Dallas R. Trinkle,[3] and Richard G. Hennig[2,1,*]

[1]*Department of Materials Science and Engineering, Cornell University, Ithaca, New York 14853, USA*

[2]*Department of Materials Science and Engineering, University of Florida, Gainesville, Florida 32611, USA*

[3]*Department of Materials Science and Engineering, University of Illinois, Urbana-Champaign, Illinois 61801, USA*

[4]*Federal Institute of Materials Research and Testing (BAM), 12205 Berlin, Germany*

(Received 4 August 2017; revised 1 August 2020; accepted 27 August 2020; published 14 October 2020)

One of the most ubiquitous and important defects in solids is oxygen. Knowledge about the solubility and diffusivity of oxygen in materials is crucial to understand a number of important technological processes, such as oxidation, corrosion, and heterogeneous catalysis. Density-functional theory calculations of the thermodynamics and kinetics of oxygen in cobalt show that oxygen diffusing into the two close-packed phases, namely α (hcp) and β (fcc), strongly interacts with vacancies. We observe the formation of oxygen split-vacancy centers (V-O_i-V) in both phases, and we show that this defect complex exhibits a similar migration energy barrier to the vacancy and oxygen interstitials. In contrast to the vacancy and oxygen interstitials, the oxygen split-vacancy centers exhibit an anisotropic strain field that couples to applied stress, making it possible to observe them through an internal friction experiment on quenched cobalt.

DOI: 10.1103/PhysRevMaterials.4.103608

I. INTRODUCTION

Point defects in solids influence the mechanical, electronic, and optical properties of these materials. Often, small changes in defect chemistry can have a large effect on the way a material behaves. In transition-metal oxides, for example, the parent compounds of the high-temperature cuprate superconductors are insulators, but the introduction of atomic point defects—either the removal of some oxygen ions or the substitution of some metal cations by others of different valence—is essential for the normal-state conductivity from which superconductivity emerges [1].

Furthermore, these defects can move around (see Fig. 1). This results in atomic transport, which can play a significant role in the synthesis and processing of materials. In iron-copper alloys, vacancies are strongly bound to copper atoms, dragging them along to facilitate the precipitation of copper around vacancy sinks [2,3]. Flux coupling can also result in the nucleation of thermodynamically unstable phases such as Ni_3Si in undersaturated Ni(Si) alloys [4].

Some of the most interesting defect complexes involve the formation of a split-vacancy center (V-X_i-V), where two adjacent lattice sites are unoccupied, and a host or impurity atom occupies the interstitial position midway between the two vacant sites. The "semivacancy pair" (V-Si_i-V) [5] and "tin-vacancy pair" (V-Sn_i-V) [6] in silicon were the first experimentally observed *self* and *impurity* split-vacancy centers, respectively. Several *self* V-X_i-Vs have been observed since in pyrochlores and other complex oxides [7,8]. The known *impurity* V-X_i-Vs, however, are limited to metal impurity atoms in open diamond structures [9]. The formation of such *impurity* defect complexes has been attributed to the argument of strain relaxation of oversized impurities upon movement to the more spacious interstitial sites [9].

One of the most ubiquitous and important defects in solids is oxygen (O), which strongly reacts with most metals to form oxides. Many recent studies have shown that metal-oxygen systems exhibit a rich and complex surface phase space determined by pressure, temperature, and stoichiometry [10,11]. Clearly, a precise knowledge of the detailed atomic structure of these systems is desired to improve our control of important technological processes such as oxidation, corrosion, and heterogeneous catalysis, which involve interaction between metals and oxygen [12].

Cobalt (Co) and its oxides have recently received considerable attention for their applications in gas sensing, heterogeneous catalysis, intercalation compounds for energy storage, electrochromic devices, and as thermoelectric materials [13–17]. Co has a rich phase diagram with three nearly degenerate crystal structures: α-Co (hcp), β-Co (fcc), and ϵ-Co (cubic) [18]. Under ambient conditions, cobalt crystallizes into α-Co [19]. Upon heating, the hcp phase transforms to the fcc β-Co structure at $\sim$700 K, which is then stable all the way up to the melting temperature of $\sim$1770 K [19]. The ϵ-Co phase possesses a more complex structure, and its synthesis has only been possible through solution-phase chemistry processes [20,21]. All three phases are ferromagnetic; however, a Curie temperature (T_c = 1388 K) has been defined only for the fcc β-Co phase [19] since both α-Co and ϵ-Co transform to the fcc phase before achieving a paramagnetic structure.

Even though we have detailed knowledge about the structure, properties, and processing of different Co phases, very little is known about the thermodynamics and kinetics of O in Co. In this work, we use density-functional theory (DFT) to show that both close-packed phases of Co display complex

*rhennig@ufl.edu

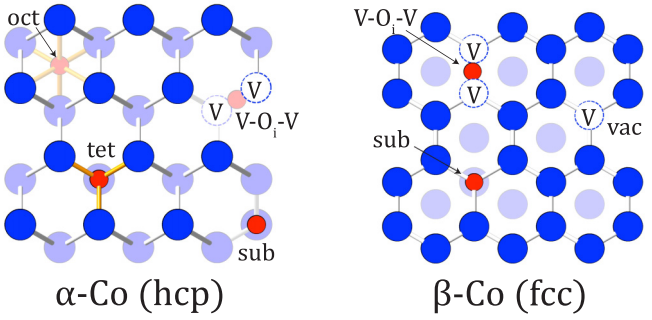

FIG. 1. Defects in α-Co (hcp) and β-Co (fcc) shown with the help of blue (cobalt), red (oxygen), and hollow (vacancy) circles. Depth fading is used to make atoms that lie further back appear lighter.

defect structures in the presence of O (see Fig. 1), affecting the transport of O as well as of vacancies (V) in Co. We first predict the equilibrium point defect structures for O, V, and their complexes in α-Co and β-Co, and then we determine how these defects migrate through the crystal structures. We show that O has a high solubility and diffusivity as an interstitial (O_i). Surprisingly, however, O_i strongly reacts with V to form split-vacancy centers (V-O_i-V), which provide an alternate pathway for O and V diffusion in Co. We show that these V-O_i-Vs exhibit an anisotropic strain field that couples to applied stress, in contrast to the isotropic strain fields of the individual V and O_i defects. This leads to a behavior similar to the observed Snoek effect for carbon and nitrogen in bcc Fe [22], and it allows for the experimental detection of these complexes by internal friction measurements.

II. METHODS

We perform the DFT calculations with the projector augmented wave method [23,24] as implemented in the VASP code [25–28] using the gradient-corrected PBE exchange-correlation functional [29]. Calculations are carried out with periodic boundary conditions, with wave functions expanded on a plane-wave basis set. The energy cutoff and the corresponding cutoff for the augmentation functions are set to 400 and 650 eV, respectively, to ensure convergence of the total energy to within 1 meV/at. The k-point integration of the Brillouin zone is performed using Monkhorst and Pack meshes [30] with a density of 30 k-points per inverse Ångström. We use spin polarization to account for the magnetism in these materials. We also constrain the cell shape and volume for all defect calculations to those of the relaxed bulk phases.

For a defect-mediated diffusion mechanism, the activation energy of diffusion, $E^{\mathrm{act}}_{\mathrm{def}}$, is given by the sum of the defect formation energy, $E^{\mathrm{f}}_{\mathrm{def}}$, and the defect migration energy barrier, $E^{\mathrm{m}}_{\mathrm{def}}$. We calculate the migration barriers with the climbing image nudged elastic band (NEB) method [31,32] using one to three intermediate images to describe the transition pathways between neighboring lattice and interstitial defect sites. We look at simple paths as well as more complex ones involving a concerted movement of multiple species. Comparing the total activation energies for competing mechanisms helps us to determine the dominant diffusion processes controlling the kinetics in these systems.

TABLE I. Finite-size effects on the defect formation energies ($E^{\mathrm{f}}_{\mathrm{def}}$) in cobalt. We find that $E^{\mathrm{f}}_{\mathrm{def}}$ is accurate to within 0.03 eV for larger supercells.

Defect	Structure	Supercell size	N_{atoms}	$E^{\mathrm{f}}_{\mathrm{def}}$ (eV)
V_{Co}	α (hcp)	$2\times2\times2$	16	1.87
		$3\times3\times2$	36	1.94
		$4\times4\times3$	96	1.92
V-O_i-V	β (fcc)	$3\times3\times3$	27	2.58
		$4\times4\times4$	64	2.52
		$5\times5\times5$	125	2.49

III. FINITE-SIZE ERROR OF DEFECT ENERGIES

The formation energies of defects in DFT calculations that employ periodic boundary conditions are affected by the size of the unit cell. Table I and Fig. 2 compare the effects of varying cell size on defect formation energies. To reduce finite-size effects, we choose our unit cells to be as large as possible while being computationally feasible. We use a $4\times4\times3$ supercell (96 atoms) of α-Co and a $5\times5\times5$ supercell (125 atoms) of β-Co for all our calculations, which provide defect formation energies accurate to within 0.03 eV.

IV. DEFECT STABILITY

To determine the stability of point defects in Co, we calculate formation energies for (i) a vacancy on a cobalt site (V_{Co}), (ii) a substitutional oxygen atom on a cobalt site (O_{Co}), (iii) a substitutional oxygen atom and a neighboring vacancy ($O_{Co}+V_{Co}$), (iv) an oxygen atom on an interstitial site (O_i), and (v) a cobalt atom on an interstitial site (Co_i). We use the chemical potential of oxygen in rocksalt CoO as a reference.

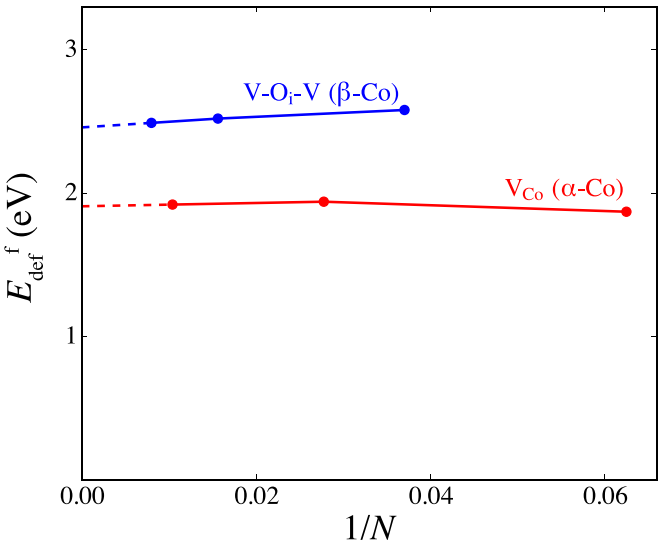

FIG. 2. Finite-size effects on the defect formation energies ($E^{\mathrm{f}}_{\mathrm{def}}$) in cobalt. We find that $E^{\mathrm{f}}_{\mathrm{def}}$ is accurate to within 0.03 eV for larger supercells.

TABLE II. Defect formation energies (E^{f}_{def}) in cobalt. Interstitial atoms in hcp and fcc can occupy either the octahedral or tetrahedral sites. Both energies are reported (E_{oct}, E_{tet}).

Defect	α-Co (hcp)	β-Co (fcc)
V_{Co}	1.92	1.79
O_{Co}	1.84	1.92
O_{Co}+V_{Co}	2.51	2.49
O_i	0.52, 1.28	0.49, 1.25
Co_i	5.19, 4.49	4.48

Table II compares the formation energies for the various defects in α-Co and β-Co. We do not report an energy for the tetrahedral Co_i defect in β-Co as it always relaxes into an octahedral position.

We make an interesting observation for the case of a substitutional O atom sitting next to a vacancy in β-Co: the $O_{Co} + V_{Co}$ defect complex relaxes to form a highly stable V-O_i-V split-vacancy center with the O atom occupying the interstitial space between two vacancies. This is similar to the tin split-vacancy center (V-Sn_i-V) in silicon studied by Watkins *et al.* [6]. We also see that the same defect occurs in α-Co; however, the formation of V-O_i-V in the hcp phase is limited to the case in which the two neighboring vacancies lie in separate basal planes. If the neighboring vacancies occupy positions in the same basal plane, the O atom no longer relaxes to a symmetric center position.

To search for other split-vacancy centers, we extend our calculations to include the $O_{Co} + V_{Co}$ defect with V and O as second and third nearest neighbors to each other (2NN and 3NN). We observe the formation of V-O_i-V in the 2NN case but not 3NN for both α-Co and β-Co.

Table III shows the strong binding energies for the split-vacancy O defect in the 1NN and 2NN configurations in α-Co and β-Co. Even in the 3NN case, where a split-vacancy center does not form, we still see significant binding between O and V. We define the binding energy as the difference in energies between a system with interacting defects and a system with isolated defects far away from each other. A large positive binding energy implies there is a strong attraction between the individual defects. We find that the binding is equally strong in the 1NN and 2NN configurations but gets weaker as the individual defects move further apart from each other (3NN).

As stated earlier, previous research showed the occurrence of *impurity* split-vacancy centers being limited to open diamond structures thus far, where a large metal impurity atom (M) relaxed to occupy the more spacious position between

TABLE III. Binding energies (in eV) of the oxygen-vacancy complex in α-Co and β-Co for first- (1NN), second- (2NN), and third-nearest-neighbor (3NN) sites relative to the isolated defects. The symmetric V-O_i-V configuration is observed to be the most stable one for 1NN and 2NN sites in both α-Co and β-Co.

	1NN	2NN	3NN
α-Co	1.25	1.14	0.68
β-Co	1.22	1.32	0.68

TABLE IV. Diffusion activation energies for the various defects in Co. The considered mechanisms include Co diffusing through vacancies (V_{Co}): Co_{Co}+V_{Co} → V_{Co}+Co_{Co}; O diffusing through interstitials (O_i): O_i^{oct} → O_i^{tet} → O_i^{oct}; 1NN V-O_i-V defect diffusing to 1NN V-O_i-V sites (1NN): V-O_i-V^{1NN} → V-O_i-V^{1NN} and 1NN V-O_i-V defect diffusing to 2NN V-O_i-V sites (2NN): V-O_i-V^{1NN} → V-O_i-V^{2NN}.

Diffusion	α-Co (hcp)			β-Co (fcc)		
	E^{f}_{def}	E^{m}_{def}	E^{act}_{def}	E^{f}_{def}	E^{m}_{def}	E^{act}_{def}
V_{Co}	1.92	0.86	2.78	1.79	1.00	2.79
O_i	0.52	0.91	1.43	0.49	0.99	1.48
V-O_i-V (1NN)	2.51	0.90	3.41	2.49	0.91	3.40
V-O_i-V (2NN)	2.51	1.31	3.82	2.49	1.38	3.87

two neighboring vacancies (V-M_i-V). The reason for the formation of such complexes was not completely understood. The argument of strain relaxation of oversized impurities that was proposed to explain the formation of the Sn-V complex in Si [9] does not fit our description of a smaller O atom forming a similar complex in close-packed Co. While strain probably plays a role, we believe there might also be other factors at play. On closer examination, we see that O sits on a distorted octahedral site in the V-O_i-V configuration, albeit with two missing Co neighbors. This resembles the geometry and coordination in the rocksalt CoO phase that would form with sufficient O present. The Co-O distance in the V-O_i-V configuration is found to be 2.0 Å, which is intermediate between the Co-O distances in the interstitial and substitutional configuration of 1.9 and 2.5 Å, and closer to the value for CoO of 2.1 Å. This suggests that strain coupled with the natural tendency of the impurity O atoms to stabilize into a CoO-like local configuration might explain the formation of these O split-vacancy centers in Co.

V. DEFECT REACTIONS AND MIGRATION

Next, we calculate migration barriers for Co and O atoms diffusing from one defect site to another to infer the most likely mechanism for diffusion in α-Co and β-Co. We identify mechanisms of diffusion for Co through vacancies, and for O through vacancies and interstitial sites. Table IV lists the formation energies, migration barriers, and total activation energies for the various defects in Co. We find that the migration barriers for diffusion through the two close-packed phases are surprisingly similar for V_{Co}, O_i, and V-O_i-V. For the oxygen interstitial, we find that the octahedral-tetrahedral-octahedral interstitial path exhibits the lowest migration energy barrier. Figures 3 and 4 illustrate the diffusion pathways of the 1NN V-O_i-V defect through other 1NN V-O_i-V and 2NN V-O_i-V sites.

Finally, we combine the defect formation energies with knowledge of the migration barriers to obtain a complete picture of the diffusion of O in Co (Table IV). The formation energies indicate that O prefers to sit on the O_i sites in Co. Not only does O have the highest solubility on such sites, but it also has a small migration barrier to move between them, providing what appears to be the fastest mechanism for O diffusion in Co. If such an O_i were to encounter a V_{Co},

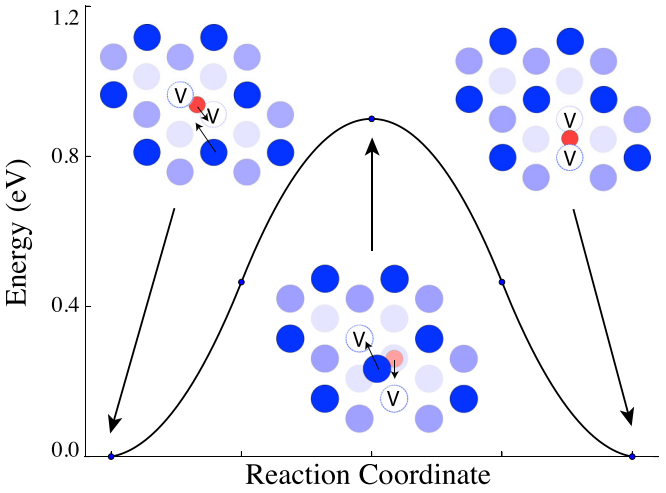

FIG. 3. Diffusion between two neighboring 1NN oxygen split-vacancy centers (V-O_i-V) is shown for β-Co (fcc). This mechanism involves a concerted motion of Co and O atoms.

however, they can exothermally combine to form O_{Co},

$$O_i + V_{Co} \rightleftharpoons O_{Co}. \tag{1}$$

The reaction energies are -0.60 and -0.36 eV in α-Co and β-Co, respectively. This substitutional O_{Co} can only move when it encounters another V_{Co}, at which point they combine exothermally to form the V-O_i-V split-vacancy center,

$$O_{Co} + V_{Co} \rightleftharpoons \text{V-O}_i\text{-V}, \tag{2}$$

with a reaction energy of -1.25 and -1.22 eV in α-Co and β-Co, respectively. Table IV shows that the migration barriers for V-O_i-V are similar to the barriers for O_i and V_{Co}, suggesting that the formation of V-O_i-V complexes does not trap oxygen and vacancies, and that V-O_i-V diffusion could provide an alternate mechanism for O and Co transport through close-packed Co.

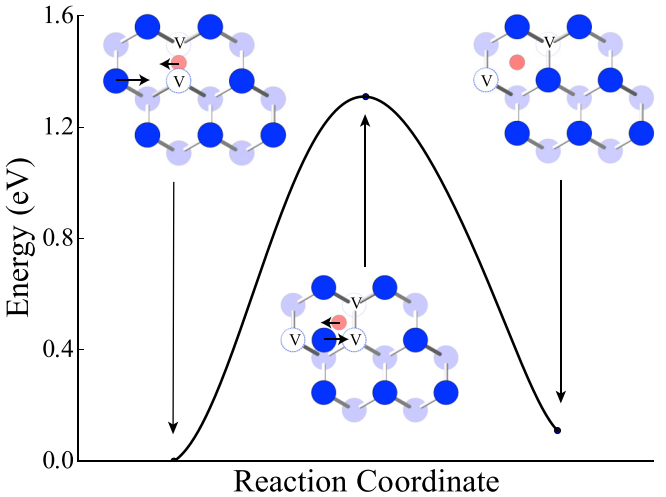

FIG. 4. Diffusion between a 1NN and 2NN oxygen split-vacancy center (V-O_i-V) is shown for α-Co (hcp). This mechanism involves a concerted motion of Co and O atoms.

To experimentally detect the presence of V-O_i-V complexes, they must form in sufficient concentrations, which will depend on the processing of the material. To determine the equilibrium concentration of the V-O_i-V defects, we obtain the equilibrium constant for the combined reaction of Eqs. (1) and (2),

$$O_i + 2V_{Co} \rightleftharpoons \text{V-O}_i\text{-V}, \tag{3}$$

$$K_{eq} = \exp\left(-\frac{\Delta E}{kT}\right) = \frac{[\text{V-O}_i\text{-V}]}{[O_i][V_{Co}]^2}. \tag{4}$$

The concentration of V-O_i-V is clearly limited by the total number of V_{Co} in our system, since two vacancies are needed to form every split-vacancy center. Using the vacancy formation energy for β-Co, we estimate the room-temperature equilibrium concentration of vacancies, $[V_{Co}] = 9 \times 10^{-31}$, implying a negligibly small concentration of V-O_i-V.

The vacancy concentration in a material can generally be increased by quenching from high temperature or by irradiation. A quench from 1700 K, just below the melting point of 1770 K, to 700 K increases $[V_{Co}]$ in β-Co to 5×10^{-6}. Assuming the quenched vacancy concentration and the oxygen concentration of 1×10^{-3} are fixed in the bulk of the sample away from any sources or sinks, we calculate the equilibrium concentration of V-O_i-V at 700 K to be 2.45×10^{-6}. This result, namely that at intermediate temperatures essentially all vacancies are bound in the form of the V-O_i-V complexes, is a direct consequence of the significantly higher reaction energy of the reaction in Eq. (2).

For V-O_i-V to form, the O_i and V_{Co} must also encounter each other fairly quickly. For $[V_{Co}] = 5 \times 10^{-6}$, we estimate the time scale for the encounters at 700 K to be of a few ms according to

$$\langle R_n^2 \rangle = nr^2 = t\Gamma r^2 = 6Dt, \tag{5}$$

where $\langle R_n^2 \rangle$ is the mean-square displacement after time t, n is the number of jumps, r is the individual jump length, Γ is the jump frequency, and D is the diffusion coefficient. This timescale is sufficiently short to convert all V_{Co} into V-O_i-V split-vacancy centers during the quench while avoiding thermal equilibration of the vacancy concentration at grain boundaries and interfaces. We conclude that as long as there is a sufficient number of quenched V_{Co}, and mobile O_i encounter the V_{Co}, V-O_i-V will form even against the observed formation energy trend in Table II.

VI. INTERNAL FRICTION

The experimental assessment of a damping mechanism in metals has a long history [33], where cross-comparison between different reported damping mechanisms is not always easy since each particular measurement technique is limited to a given frequency range. Consequently, most experiments have been done in different frequency regimes and over a range of temperatures that is either above or below room temperature.

In the particular case of damping due to interstitials, considerable efforts have been dedicated to studying hydrogen (H), oxygen (O), or nitrogen (N) in bcc lattices [34,35],

whereas hcp lattices, and in particular Co, have been less commonly investigated. However, a series of earlier studies using the torsion pendulum method, often operated at frequencies at or close to 1 Hz, were dedicated to interstitial site relaxation processes in hcp crystals [36–40]. This body of experimental work reports mechanical relaxation that occurs in the range of 700–750 K, depending on the metal (Ti, Hf, Zr). This temperature range overlaps with the allotropic phase transition from α-Co to β-Co and may be the main reason for the lack of experimental evidence of Snoek-type losses.

In the case of Ti, Pratt *et al.* reported that the purest polycrystalline grade only exhibits an internal friction signature from grain-boundary processes [36], whereas the careful introduction of 1.5–4.5 at. % O revealed a relaxation peak at ∼700 K, the magnitude of which was proportional to the O-content. Qualitatively, the same was reported for reactor-grade Hf (containing 6 wt. % Zr) by Bisogni *et al.* [38], where the loss process is seen at ∼750 K and a frequency of 0.9 Hz. These experimental observations were in contrast to the conclusion that losses of Snoek type ought not to be seen for interstitials in fcc or hcp due to the geometry of the octahedral and tetrahedral site [38], where O is expected to occupy the former because of its atomic size. Gupta and Weinig convincingly addressed this discrepancy experimentally by demonstrating that substitutional impurities are the cause for the observed damping. Due to the local lattice distortion caused by the substitutional element, the relaxation of an interstitial-solute (i-s) pair was consequently shown to depend on the relative atomic size mismatch between the base element and the solute and scale with solute concentration at constant O-content [37]. Interstitial-interstitial (i-i) pair relaxation had been theoretically predicted [41], and was subsequently shown for dilute Ti, Hf, and Zr alloys [40] in the aforementioned temperature range. These experimental efforts have in common that they use low-frequency excitations and study a temperature regime from room temperature to ∼875 K and are limited to Ti, Hf, and Zr.

With a view to experimentally confirm the presence of V-O_i-V and study its diffusion, we determine how the defect couples to applied stress in β-Co. The V-O_i-V complexes in β-Co are oriented along any of the ⟨110⟩ directions, producing six different orientations ([110] and $[\bar{1}\bar{1}0]$ are identical). The derivative of the defect energy with respect to strain is the elastic dipole tensor, $\underline{P}$. For the case of a V-O_i-V defect oriented along the [110] direction, we find

$$\underline{P} = \begin{pmatrix} -2.70 & 0.13 & 0 \\ 0.13 & -2.70 & 0 \\ 0 & 0 & -4.30 \end{pmatrix} \text{GPa}. \tag{6}$$

This dipole tensor indicates an anisotropic compression of the structure. The compression is expected for a defect involving two vacancies. The anisotropy of the dipole tensor is a necessary ingredient for internal friction loss due to an oscillating applied stress. The largest coupling to applied stress is due to the difference between the "in-plane" (−2.70 GPa) normal component and the "out-of-plane" (−4.30 GPa) normal component, which can couple to either uniaxial or shear stresses differently for each of the 12 ⟨110⟩ V-O_i-V complexes. The in-plane shear component (0.13 GPa) is an order of magnitude smaller and plays a negligible role in internal friction. The appendix provides a detailed derivation of the loss due to internal friction. The loss Q^{-1} depends on the jump rate $\lambda = \nu_0 \exp(-E^{\text{m}}_{\text{def}}/k_{\text{B}}T)$, where $E^{\text{m}}_{\text{def}} = 0.91$ eV (Table IV); only one eigenvalue of the transition matrix couples strongly to shear strains, so

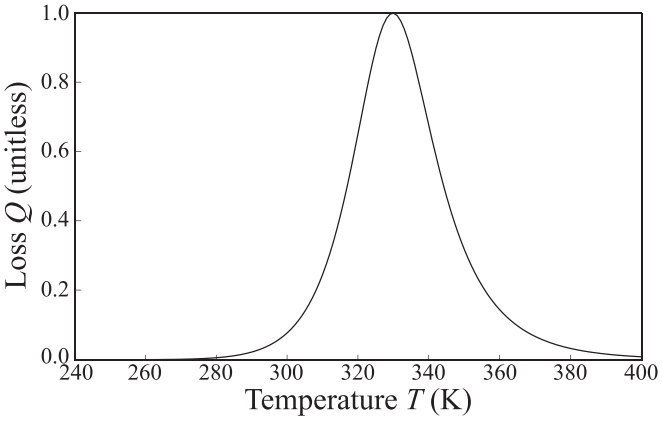

FIG. 5. Predicted internal friction loss per cycle at $\nu = 1$ Hz due to V-O_i-V complexes in β-Co. Under a cyclic nonhydrostatic load, the lowered symmetry of the complexes produces different changes in energy for different sites; this drives transitions from higher to lower energy states, producing loss in energy, similar to the Snoek effect from C in bcc-Fe. The loss is proportional to the concentration of V-O_i-V, and it reaches a peak near 330 K.

$$Q^{-1} \propto \frac{[\text{V-O}_i\text{-V}]}{k_{\text{B}}T} \frac{12\lambda\nu}{\nu^2 + (12\lambda)^2}, \tag{7}$$

which is plotted in Fig. 5. The prediction for internal friction shows that for a torsional pendulum of a quenched Co wire with $\nu = 1$ Hz, the peak loss Q^{-1} corresponding to maximum damping should occur near 330 K.

Snoek-type relaxations in Co remain experimentally unexplored, but the consistently observed features for other hcp metals suggest that similar i-s and i-i mechanisms could occur in Co. It is worth noting that torsion pendulum data recorded when studying the hcp-fcc transition at 0.5 Hz in Co displays at least one unexplored small peak at ∼550 K during both cooling and heating [42]. The room-temperature loss mechanism theoretically predicted here was not identified in any of the studied hcp metals; it may find its origin in the continuously increasing damping with temperature that will drown small-amplitude peaks at the low-temperature end. Additional experimental efforts that carefully examine low-frequency excitations at and around room temperature are thus critically needed so as to test our predictions and to potentially identify a loss mechanism that is generic to hcp lattices that contain solved O.

VII. CONCLUSION

We performed DFT calculations to measure the formation energies and migration barriers of O point defects in α (hcp) and β (fcc) cobalt. We predict that in both phases O strongly interacts with vacancies to form oxygen split-vacancy

centers V-O_i-V in the presence of sufficiently high vacancy concentrations. We show that the oxygen split-vacancy centers do not trap oxygen, and they provide an alternate mechanism for oxygen diffusion in close-packed cobalt. We propose a way to observe and measure their diffusion through an internal friction experiment. We show that the oxygen split-vacancy centers exhibit an anisotropic strain field, in contrast to the isolated vacancies and oxygen interstitials. This strain field couples to applied stress, and the diffusion of V-O_i-V leads to a maximum damping in internal friction at experimentally accessible frequencies and temperatures. Similar split-vacancy centers may also occur for oxygen and other interstitial species in various close-packed materials.

ACKNOWLEDGMENTS

This work was supported by the National Science Foundation under Awards No. ACI-1440547 and No. CHE-1665310. This research used computational resources provided by the University of Florida Research Computing [43] and the Texas Advanced Computing Center under Contracts No. TG-DMR050028N, No. TG-DMR140143, and No. TG-DMR150006. This work used the Extreme Science and Engineering Discovery Environment (XSEDE), which is supported by National Science Foundation Grant No. ACI-1053575.

APPENDIX: LOSS UNDER CYCLIC LOADING

1. Definitions

To consider the energy loss per cycle under mechanical load due to transitions between defect sites, we use the nomenclature introduced for the derivation of transport coefficients for interstitial defects [44]. We have a set of N defects in our unit cell that can be indexed using $i = 1, \ldots, N$, and where a series of possible transitions between these defects are possible. For a defect state i in the unit cell, it has an equilibrium site probability ρ_i that follows the Arrhenius relationship,

$$\rho_i := cZ^{-1}\rho_i^0 \exp\left(-\beta E_i\right) \tag{A1}$$

for site energy E_i, concentration per unit cell c, entropic prefactor $\rho_i^0 = \exp(S_i/k_\mathrm{B})$, and partition function $Z = \sum_i \rho_i^0 \exp\left(-\beta E_i\right)$. The transition from site i to site j has a rate $\lambda_{i\to j}$,

$$\lambda_{i\to j} := \frac{\lambda_{ij}^0}{\rho_i^0} \exp\left(-\beta\left[E_{ij}^{\mathrm{ts}} - E_i\right]\right) \tag{A2}$$

for transition state energy E_{ij}^{ts} and entropic prefactor $\lambda_{ij}^0 = \exp(S_{ij}^{\mathrm{ts}}/k_\mathrm{B})$, following [45]. In this formulation, the transition state energy and entropic prefactors are equal for $i \to j$ and for $j \to i$, while it is not necessary that $\lambda_{i\to j}$ and $\lambda_{j\to i}$ are equal. Finally, the probabilities obey detailed balance, where $\rho_i\lambda_{i\to j} = \rho_j\lambda_{j\to i}$ for all i, j.

We will assume that the stress amplitude is sufficiently small that we are in a linear elastic regime, there is a small defect concentration, and the energy loss is a small perturbation in the system energy. The dilute limit permits us to ignore defect-defect interactions. The linear elastic limit allows us to transform from a stress amplitude into a strain amplitude, and to write the changes to our site probabilities and transition rates to first order in the strain using the elastic dipole. The elastic dipole tensor $\underline{P}_i$ for a site i is

$$\underline{P}_i := -\frac{dE_i}{d\underline{\varepsilon}}. \tag{A3}$$

The elastic dipole can be conveniently evaluated in a supercell calculation from the stress in the cell: an interstitial is added to an initially undefected, unstressed supercell containing N atoms (with equilibrium volume V_0 per atom), resulting in a stress $\underline{\sigma}$, then to first order in N^{-1},

$$\underline{P} \approx NV_0\underline{\sigma}, \tag{A4}$$

which is straightforward to evaluate with density-functional theory methods, e.g., see [46–49]. Similarly, the energy of a transition state can also change with strain, as dictated by the elastic dipole tensor for the transition state $\underline{P}_{ij}^{\mathrm{ts}}$ for the transition state between i and j,

$$\underline{P}_{ij}^{\mathrm{ts}} := -\frac{dE_{ij}^{\mathrm{ts}}}{d\underline{\varepsilon}}. \tag{A5}$$

This, too, can be approximated by the stress at the transition state in a supercell calculation as in Eq. (A4); e.g., see [48,50]. The definitions of elastic dipoles allow the introduction of a small strain perturbation $\delta\underline{\varepsilon}$ to produce site energy changes δE_i and transition energies $\delta E_{ij}^{\mathrm{ts}}$ as

$$\begin{aligned} \delta E_i &= -\underline{P}_i : \delta\underline{\varepsilon}, \\ \delta E_{ij}^{\mathrm{ts}} &= -\underline{P}_{ij}^{\mathrm{ts}} : \delta\underline{\varepsilon}, \end{aligned} \tag{A6}$$

which is correct to first order in strain.

2. Master equation

The evolution of the defects is defined by the Master equation, and we can include the effect of a (perturbative) time-dependent strain. The time-dependent occupancy $c_i(t)$ of site i is given by

$$\frac{dc_i}{dt} = \sum_j \lambda_{j\to i}c_j(t) - \lambda_{i\to j}c_i(t). \tag{A7}$$

We introduce the rate matrix Λ_{ij},

$$\Lambda_{ij} := \begin{cases} \lambda_{i\to j} & : i \neq j, \\ -\sum_j \lambda_{i\to j} & : i = j, \end{cases} \tag{A8}$$

and so Eq. (A7) is simply $\dot{c} = c\Lambda$. By detailed balance, the equilibrium site probability ρ satisfies $\rho\Lambda = 0$. Similar to our expressions for changes in site and transition energies, a small strain introduces a change in the rate matrix $\delta\Lambda_{ij} : \delta\underline{\varepsilon}$,

$$\delta\Lambda_{ij} : \delta\underline{\varepsilon} := \begin{cases} \lambda_{i\to j}(k_\mathrm{B}T)^{-1}(\underline{P}_{ij}^{\mathrm{ts}} - \underline{P}_i) : \delta\underline{\varepsilon} & : i \neq j, \\ -\sum_j \lambda_{i\to j}(k_\mathrm{B}T)^{-1}(\underline{P}_{ij}^{\mathrm{ts}} - \underline{P}_i) : \delta\underline{\varepsilon} & : i = j, \end{cases} \tag{A9}$$

based on Eq. (A2). If we consider that our system is close to equilibrium, so that

$$c_i(t) = \rho_i + \underline{F}_i : \delta\underline{\varepsilon}(t), \tag{A10}$$

then the (time-dependent) Master equation in the perturbative limit is

$$\begin{aligned}\underline{F}_i : \delta\dot{\underline{\varepsilon}}(t) &= \sum_j [\rho_j + \underline{F}_j : \delta\underline{\varepsilon}(t)][\Lambda_{ji} + \delta\Lambda_{ji} : \delta\underline{\varepsilon}(t)] \\ &= \sum_j (\underline{F}_j \Lambda_{ji}) : \delta\underline{\varepsilon}(t) + \sum_j \rho_j \delta\Lambda_{ji} : \delta\underline{\varepsilon}(t) + O(\delta\underline{\varepsilon}^2). \end{aligned} \tag{A11}$$

This can be solved for a cyclic strain $\delta\underline{\varepsilon}(t) = \delta\underline{\varepsilon}_0 e^{i\nu t}$ with frequency ν, so that $\delta\dot{\underline{\varepsilon}}(t) = i\nu\ \delta\underline{\varepsilon}(t)$, and we have

$$\begin{aligned}\sum_j \underline{F}_j (i\nu\delta_{ji} - \Lambda_{ji}) &= \sum_j \rho_j \delta\Lambda_{ji} \\ \underline{F}_i &= \sum_{jk} \rho_j \delta\Lambda_{jk} (i\nu\mathbf{1} - \Lambda)^{-1}_{ki}. \end{aligned} \tag{A12}$$

The first term in the sum, $\sum_j \rho_j \delta\Lambda_{jk}$, simplifies as

$$\begin{aligned}\sum_j \rho_j \delta\Lambda_{jk} &= \sum_j \rho_j \lambda_{j\to k} (k_\mathrm{B}T)^{-1} \left(\underline{P}^{\mathrm{ts}}_{jk} - \underline{P}_j\right) - \sum_j \rho_k \lambda_{k\to j} (k_\mathrm{B}T)^{-1} \left(\underline{P}^{\mathrm{ts}}_{kj} - \underline{P}_k\right) \\ &= (k_\mathrm{B}T)^{-1} \sum_j \rho_j \lambda_{j\to k} \left[\underline{P}^{\mathrm{ts}}_{jk} - \underline{P}_j - \underline{P}^{\mathrm{ts}}_{kj} + \underline{P}_k\right] = -(k_\mathrm{B}T)^{-1} \sum_j \rho_j \underline{P}_j \Lambda_{jk} \end{aligned} \tag{A13}$$

so that Eq. (A12) becomes

$$\underline{F}_i = -(k_\mathrm{B}T)^{-1} \sum_{jk} \rho_j \underline{P}_j \Lambda_{jk} (i\nu\mathbf{1} - \Lambda)^{-1}_{ki}. \tag{A14}$$

To compute the loss per cycle, we integrate the time derivative of the energy multiplied by the instantaneous occupancy of each site over one cycle. The time derivative of energy is the work done on each defect, which is at the expense of the elastic energy in the system. The instantaneous energy of each site is $E_i(t) = \mathrm{Re}(E_i - \underline{P}_i : \delta\underline{\varepsilon}_0 e^{i\nu t})$, while $c_i(t) = \mathrm{Re}(\rho_i + \underline{F}_i : \delta\underline{\varepsilon}_0 e^{i\nu t})$, and so

$$-\sum_i c_i(t)\dot{E}_i(t) = -\sum_i (\rho_i + \mathrm{Re}\underline{F}_i : \delta\underline{\varepsilon}_0 \cos(\nu t) - \mathrm{Im}\underline{F}_i : \delta\underline{\varepsilon}_0 \sin(\nu t))(\nu\underline{P}_i : \delta\underline{\varepsilon}_0 \sin(\nu t)). \tag{A15}$$

We integrate the change in energy over one cycle to find

$$\begin{aligned}\Delta E_{\mathrm{cycle}} &= -\int_0^{2\pi\nu^{-1}} dt \sum_i c_i(t)\dot{E}_i(t) \\ &= \int_0^{2\pi\nu^{-1}} dt \sum_i [(\underline{P}_i : \delta\underline{\varepsilon}_0)(\mathrm{Im}\underline{F}_i : \delta\underline{\varepsilon}_0)\nu \sin^2(\nu t)] \\ &= \pi \sum_i (\delta\underline{\varepsilon}_0 : \underline{P}_i)(\mathrm{Im}\underline{F}_i : \delta\underline{\varepsilon}_0). \end{aligned} \tag{A16}$$

To convert this to a fractional loss per cycle, we need to divide by the *elastic* energy per cycle, which is $\pi\Omega_0 \delta\underline{\varepsilon}_0 : \underline{C} : \delta\underline{\varepsilon}_0$, for the elastic constant tensor $\underline{C}$ and volume per unit cell Ω_0.

We can find the solution for the loss by eigendecomposing the matrix Λ, and rewriting Eqs. (A14) and (A16) in terms of its eigenvectors and values. While the matrix Λ is generally not symmetric, the matrix

$$\omega_{ij} := \rho_i^{1/2} \Lambda_{ij} \rho_j^{-1/2} \tag{A17}$$

is. Moreover, it is a negative semidefinite matrix, with exactly one zero eigenvalue; let r^n be the real, negative eigenvalues where $r^0 = 0$, and let s^n be the corresponding eigenvectors, where $s^0_i = \rho_i^{1/2}$. As $\Lambda_{ij} = \rho_i^{-1/2} \omega_{ij} \rho_j^{1/2}$, it follows that

$$\sum_k \Lambda_{jk} (i\nu\mathbf{1} - \Lambda)^{-1}_{ki} = \sum_n \frac{r^n}{i\nu - r^n} \rho_j^{-1/2} s^n_j s^n_i \rho_i^{1/2}. \tag{A18}$$

We note that

$$\mathrm{Im}\frac{r^n}{i\nu - r^n} = -\frac{\nu r^n}{\nu^2 + (r^n)^2} \tag{A19}$$

and so the fourth-rank tensor in Eq. (A16) is

$$\underline{\underline{\mathcal{L}}}(\nu, T) := \sum_i \underline{\underline{P}}_i \otimes \mathrm{Im}\underline{\underline{F}}_i = (k_\mathrm{B}T)^{-1} \sum_{n>0} \frac{\nu r^n}{\nu^2 + (r^n)^2} \left(\sum_i \rho_i^{1/2} s_i^n \underline{\underline{P}}_i \right) \otimes \left(\sum_i \rho_i^{1/2} s_i^n \underline{\underline{P}}_i \right), \tag{A20}$$

which is symmetric and negative-definite, as $r^n < 0$ for all $n > 0$, and hence the loss per cycle Q^{-1} is

$$Q^{-1} = -\frac{\delta\underline{\underline{\varepsilon}}_0 : \underline{\underline{\mathcal{L}}}(\nu, T) : \delta\underline{\underline{\varepsilon}}_0}{\Omega_0 \delta\underline{\underline{\varepsilon}}_0 : \underline{\underline{C}} : \delta\underline{\underline{\varepsilon}}_0}. \tag{A21}$$

Note that the temperature dependence appears explicitly in Eq. (A20) and in the temperature dependence of the rates in Λ, and hence r^n and s^n. There is a linear dependence in concentration c from the linear dependence of ρ_i in Eq. (A20).

3. Isotropic representation

The fourth-rank loss tensor $\underline{\underline{\mathcal{L}}}$ can be simplified by converting to rotationally averaged scalar quantities: bulk $\mathcal{L}^\mathrm{b}$, shear $\mathcal{L}'$, and uniaxial $\mathcal{L}^\mathrm{u}$ corresponding to bulk, shear, or uniaxial strains in a random polycrystal,

$$\begin{aligned}
\mathcal{L}^\mathrm{b} &= \tfrac{1}{9}\{\mathcal{L}_{1111} + \mathcal{L}_{2222} + \mathcal{L}_{3333} + 2\mathcal{L}_{1122} + 2\mathcal{L}_{1133} + 2\mathcal{L}_{2233}\}, \\
\mathcal{L}' &= \tfrac{1}{5}\left\{\tfrac{1}{3}(\mathcal{L}_{1111} + \mathcal{L}_{2222} + \mathcal{L}_{3333} - \mathcal{L}_{1122} - \mathcal{L}_{1133} - \mathcal{L}_{2233}) + \mathcal{L}_{1212} + \mathcal{L}_{1313} + \mathcal{L}_{2323}\right\}, \\
\mathcal{L}^\mathrm{u} &= \mathcal{L}^\mathrm{b} + \tfrac{4}{3}\mathcal{L}'.
\end{aligned} \tag{A22}$$

For the case of loss per cycle in a torsion pendulum, $\mathcal{L}'$ is the quantity of interest.

4. Loss for oxygen-vacancy complexes in fcc cobalt

For the case of the fcc Co oxygen-vacancy complex, the loss calculation simplifies to two eigenmodes. We can identify an oxygen-vacancy complex in an fcc material based on the positions of the oxygen atom alone, as the two neighboring vacancy positions are unique. Crystallographically, this is similar to the "crowdion" interstitial defect. In the space group of fcc ($Fm\bar{3}m$), these are the d sites, of which there are six compared with the a sites for the solvent atoms. These sites, in Cartesian coordinates, are

$$\begin{array}{cccc}
(0, \frac{1}{4}, \frac{1}{4}) & (0, \frac{3}{4}, \frac{3}{4}) & (\frac{1}{2}, \frac{1}{4}, \frac{3}{4}) & (\frac{1}{2}, \frac{3}{4}, \frac{1}{4}) \\
(0, \frac{3}{4}, \frac{1}{4}) & (0, \frac{1}{4}, \frac{3}{4}) & (\frac{1}{2}, \frac{3}{4}, \frac{3}{4}) & (\frac{1}{2}, \frac{1}{4}, \frac{1}{4}) \\
(\frac{1}{4}, 0, \frac{1}{4}) & (\frac{1}{4}, \frac{1}{2}, \frac{3}{4}) & (\frac{3}{4}, 0, \frac{3}{4}) & (\frac{3}{4}, \frac{1}{2}, \frac{1}{4}) \\
(\frac{1}{4}, 0, \frac{3}{4}) & (\frac{1}{4}, \frac{1}{2}, \frac{1}{4}) & (\frac{3}{4}, 0, \frac{1}{4}) & (\frac{3}{4}, \frac{1}{2}, \frac{3}{4}) \\
(\frac{1}{4}, \frac{1}{4}, 0) & (\frac{1}{4}, \frac{3}{4}, \frac{1}{2}) & (\frac{3}{4}, \frac{1}{4}, \frac{1}{2}) & (\frac{3}{4}, \frac{3}{4}, 0) \\
(\frac{3}{4}, \frac{1}{4}, 0) & (\frac{3}{4}, \frac{3}{4}, \frac{1}{2}) & (\frac{1}{4}, \frac{1}{4}, \frac{1}{2}) & (\frac{1}{4}, \frac{3}{4}, 0).
\end{array} \tag{A23}$$

In the primitive unit cell, we only need one entry from each row, as each row represent the same *orientation*: [011], [0$\bar{1}$1], [101], [10$\bar{1}$], [110], and [$\bar{1}$10]. As all of the sites have the same energy, hence $\rho = c$. From any site, there are eight jumps that all have the same rate, λ; the transitions involve moving one of the two vacancies to a neighboring site *that is also a neighbor of the other vacancy* while it remains in place. This is equivalent to the oxygen atom displacing by $\langle \frac{1}{4}\frac{1}{4}0 \rangle$; however, only eight jumps are possible for each orientation. The transition rate matrix is

$$\Lambda = \omega = \lambda \begin{pmatrix} -8 & 0 & 2 & 2 & 2 & 2 \\ 0 & -8 & 2 & 2 & 2 & 2 \\ 2 & 2 & -8 & 0 & 2 & 2 \\ 2 & 2 & 0 & -8 & 2 & 2 \\ 2 & 2 & 2 & 2 & -8 & 0 \\ 2 & 2 & 2 & 2 & 0 & -8 \end{pmatrix}. \tag{A24}$$

The elastic dipole for a site with orientation [110] is

$$\underline{\underline{P}}_{[110]} = \begin{pmatrix} P^\parallel & P^\mathrm{s} & 0 \\ P^\mathrm{s} & P^\parallel & 0 \\ 0 & 0 & P^\perp \end{pmatrix}, \tag{A25}$$

where $P^\parallel = -2.70$ GPa, $P^\perp = -4.30$ GPa, and $P^\mathrm{s} = 0.13$ GPa. The six eigenvalues of ω are the trivial 0, the doubly degenerate -12λ, and the triply degenerate -8λ. The contributions from the -12λ eigenmodes couple to $P^\parallel - P^\perp$ while the -8λ eigenmodes couple to P^s. Because the second dipole contribution is more than an order of magnitude smaller, it does not significantly change the peak loss temperature. Both terms contribute to $\mathcal{L}'$, while $\mathcal{L}^\mathrm{b} = 0$. To identify the peak loss temperature for a single dominant eigenmode, we note that the maximum in Eq. (A20) occurs when $\nu = -r$. Writing $\lambda = \nu_0 \exp(-E^\mathrm{ts}/k_\mathrm{B}T)$, we find that the peak loss temperature at

$$T_{\max\,\mathrm{loss}} = \frac{E^\mathrm{ts}}{k_\mathrm{B} \ln(12\nu_0/\nu)}. \tag{A26}$$

For systems in which P^s was significant compared with $P^\parallel - P^\perp$, the peak loss temperature equation would change. The computational results for the damping are available at Ref. [51].

[1] J. Bednorz and K. Müller, Z. Phys. B **64**, 189 (1986).

[2] A. V. Barasheva and A. C. Arokiam, Philos. Mag. Lett. **86**, 321 (2006).

[3] T. Garnier, M. Nastar, P. Bellon, and D. R. Trinkle, Phys. Rev. B **88**, 134201 (2013).
[4] A. Barbu and A. Ardell, Scr. Metall. **9**, 1233 (1975).
[5] B. Masters, Solid State Commun. **9**, 283 (1971).
[6] G. Watkins, Phys. Rev. B **12**, 4383 (1975).
[7] M. Van Dijk, A. Burggraaf, A. Cormack, and C. Catlow, Solid State Ion. **17**, 159 (1985).
[8] D. O. Scanlon, N. M. Galea, B. J. Morgan, and G. W. Watson, J. Phys. Chem. C **113**, 11095 (2009).
[9] H. Höhler, N. Atodiresei, K. Schroeder, R. Zeller, and P. H. Dederichs, Phys. Rev. B **71**, 035212 (2005).
[10] M. Todorova, W. X. Li, M. V. Ganduglia-Pirovano, C. Stampfl, K. Reuter, and M. Scheffler, Phys. Rev. Lett. **89**, 096103 (2002).
[11] K. Reuter and M. Scheffler, Phys. Rev. Lett. **90**, 046103 (2003).
[12] C. Stampfl, M. V. Ganduglia-Pirovano, K. Reuter, and M. Scheffler, Surf. Sci. **500**, 368 (2002).
[13] J. Wöllenstein, M. Burgmair, G. Plescher, T. Sulima, J. Hildenbrand, H. Böttner, and I. Eisele, Sens. Act. B **93**, 442 (2003).
[14] Y. Okamoto, T. Imanaka, and S. Teranishi, J. Catal. **65**, 448 (1980).
[15] M. Hutchins, P. Wright, and P. Grebenik, Solar Energy Mater. **16**, 113 (1987).
[16] F. Švegl, B. Orel, M. G. Hutchins, and K. Kalcher, J. Electrochem. Soc. **143**, 1532 (1996).
[17] W. Koshibae, K. Tsutsui, and S. Maekawa, Phys. Rev. B **62**, 6869 (2000).
[18] S. Sun and C. Murray, J. Appl. Phys. **85**, 4325 (1999).
[19] T. Nishizawa and K. Ishida, Bull. Alloy phase diagrams **4**, 387 (1983).
[20] D. P. Dinega and M. Bawendi, Angew. Chem. Int. Ed. **38**, 1788 (1999).
[21] I. de PR Moreira, A. Roldán, F. Illas *et al.*, J. Chem. Phys. **133**, 024701 (2010).
[22] J. Snoek, Physica **8**, 711 (1941).
[23] P. E. Blöchl, Phys. Rev. B **50**, 17953 (1994).
[24] G. Kresse and D. Joubert, Phys. Rev. B **59**, 1758 (1999).
[25] G. Kresse and J. Hafner, Phys. Rev. B **47**, 558 (1993).
[26] G. Kresse and J. Hafner, Phys. Rev. B **49**, 14251 (1994).
[27] G. Kresse and J. Furthmüller, Comput. Mater. Sci. **6**, 15 (1996).
[28] G. Kresse and J. Furthmüller, Phys. Rev. B **54**, 11169 (1996).
[29] J. P. Perdew, K. Burke, and M. Ernzerhof, Phys. Rev. Lett. **77**, 3865 (1996).
[30] H. J. Monkhorst and J. D. Pack, Phys. Rev. B **13**, 5188 (1976).
[31] H. Jónsson, G. Mills, and K. W. Jacobsen, in *Classical and Quantum Dynamics in Condensed Phase Simulations*, edited by B. J. Berne, G. Ciccotti, and D. F. Coker (World Scientific, Singapore, 1998), pp. 385–404.
[32] G. Henkelman, B. P. Uberuaga, and H. Jónsson, J. Chem. Phys. **113**, 9901 (2000).
[33] M. S. Blanter, I. S. Golovin, H. Neuhauser, and H.-R. Sinning, *Internal Friction in Metallic Materials* (Springer, Berlin, Heidelberg, 2007).
[34] P. Schiller, Il Nuovo Cimento B **33**, 226 (1976).
[35] M. Weller, G. Haneczok, and J. Diehl, Phys. Status Solidi B **172**, 145 (1992).
[36] J. N. Pratt, W. J. Bratina, and B. Chalmers, Acta Metall. **2**, 203 (1954).
[37] D. Gupta and S. Weinig, Acta Metall. **10**, 292 (1962).
[38] E. Bisogni, G. Mah, and C. Tvert, J. Less Common Met. **7**, 197 (1964).
[39] K. M. Browne, Scripta Metall. **5**, 519 (1971).
[40] K. M. Browne, Acta Metall. **20**, 507 (1972).
[41] F. Povolo and E. A. Bisogni, Acta Metall. **14**, 711 (1966).
[42] J.-E. Bidaux, R. Schaller, and W. Benoit, Acta Metall. **37**, 803 (1989).
[43] https://www.rc.ufl.edu.
[44] D. R. Trinkle, Philos. Mag. **96**, 2714 (2016).
[45] G. H. Vineyard, J. Phys. Chem. Solids **3**, 121 (1957).
[46] Y. Hanlumyuang, P. Gordon, T. Neeraj, and D. Chrzan, Acta Mater. **58**, 5481 (2010).
[47] C. Varvenne, F. Bruneval, M.-C. Marinica, and E. Clouet, Phys. Rev. B **88**, 134102 (2013).
[48] T. Garnier, V. R. Manga, P. Bellon, and D. R. Trinkle, Phys. Rev. B **90**, 024306 (2014).
[49] H. Kim and D. R. Trinkle, Comput. Mater. Sci. **119**, 41 (2016).
[50] R. G. A. Veiga, M. Perez, C. Becquart, E. Clouet, and C. Domain, Acta Mater. **59**, 6963 (2011).
[51] D. R. Trinkle, ONSAGER, http://dallastrinkle.github.io/Onsager (2019).